Imaging plasma membrane domains in signal transduction pathways

Pezzarossa, A.

Chapter 2

Dynamic partitioning of HRas studied with high resolution imaging[1]

The plasma membrane is a highly complex, organized structure where the lateral organization of signaling proteins is believed to be tightly regulated. So far, direct visualization of membrane compartments or domains has been achieved only by electron microscopy on membrane sheets. Due to the limited resolution of light microscopy it was not possible to access such an organization on intact cells. However, recent advancement in light microscopy have made it possible to achieve unprecedented resolution. Here, we apply photo-activated light microscopy (PALM) microscopy to study the lateral organization of HRas and its minimal anchoring motif CAAX in the inner leaflet of the plasma membrane. By detailed analysis of protein distribution we confirm previous results obtained with single-molecule tracking, and further we proposed a dynamic model for HRas partitioning in and out of membrane domains. Finally, we demonstrate a coupling between the outer and inner leaflet of the plasma membrane.

[1]This chapter is based on Pezzarossa, A., Zosel, F., Schmidt, T. "Dynamic partitioning of HRas studied with high resolution imaging" (in preparation).

2.1 Introduction

The current model of the plasma membrane is that of a heterogenous bilayer, organized into microdomains that results from molecular lipid-lipid and lipid-protein interactions and further reflects the interconnections between membrane components and the actin cytoskeleton (1). Evidences of the existence of such domains in live cells, ranging in size from a few tens to about 100-200 nanometers in diameter has been found in the past decade, both through biochemical assays (2), and using sophisticated microscopy techniques including FRAP (3), FRET (4), FCS (5–7), single-particle tracking (8, 9), single-molecule microscopy (17), and by electron microscopy (10). However, a common view on their nature and their biological role is still lacking. This uncertainty in part arises from the limitations of the techniques used, as they are unable to directly observe domains in live cells. Most studies have focused on the outer leaflet of the plasma membrane by observing either labeled lipids or antibody-tagged outer membrane components which are more easily accessible experimentally. Less is known, though, about the presence of such domains in the inner leaflet of the plasma membrane, and about a possible coupling to outer leaflet domains. It is believed that such domains on the inner leaflet would act as signaling platforms and thereby play a major role in a multitude of cellular signaling pathways.

Particularly, this highly complex, organized structure with a broad range of dynamic processes is thought to have a biological role in signal transduction pathways through a tight regulation of the lateral segregation of signaling proteins. Since signals transduction involves membrane receptors, which transmit a signal from the outside to the inside through coupling with intracellular partners, a coupling between domains in the outer and inner leaflet is of extreme importance.

One of the ubiquitous pathways that involves membrane-bound proteins is the one involving Ras. Ras proteins are small GTPases that regulate cell growth and differentiation. Ras works as molecular switch between an active, GTP-bound, and an inactive, GDP-bound state in many intracellular signaling pathways. Ras proteins are localized in the cytosolic leaflet of the plasma membrane (11–13), although they can be found also in the Golgi apparatus and in the endoplasmic reticulum (14). The Ras-family comprises of various highly homologous isoforms, which significantly differ only in their C-terminal, so-called hypervariable region (HVR) (15). The HVR contains the sequence that controls how the pro-

teins anchor to the plasma membrane. Three of these isoforms, H-, N- and KRas are ubiquitously expressed in mammalian cells. Different isoforms yield different signaling outputs, although they interact with the same set of effector proteins. It has been suggested that this seeming controversy might be explained by differences in Ras localization and linked to specificity in membrane domains that might be defined by either different lipid content or structuring by the membrane skeleton.

Here we apply the stochastic superresolution imaging method of photoactivation localization microscopy (PALM), to study the partitioning of HRas and of it's minimal anchoring sequence CAAX in mouse fibroblast. By detailed analysis of the surface distribution of the proteins with 35 nm positional accuracy we were able to identify domains of increased HRas occupancy in the inner leaflet of the plasma membrane that have a size of $\approx$ 200 nm. We further show that HRas clustering on the cytosolic leaflet is enhanced by clustering of GM1 gangliosides on the extracellular leaflet by cholera toxin subunit B (CTB). HRas reorganization upon CTB administration proves the existence of a coupling between cholesterol-rich domains on the outside to nanodomains in the inside of a cell.

2.2 Materials and methods

2.2.1 Plasmids

The pDendra2 plasmid encoding for Dendra2 protein (Evrogen) was cut using the restriction sites AgeI and BSrgI. The pcDNA3.1 vector encoding for the 10 amino acids of human HRas, which includes the CAAX motif fused to YFP (17) was cut using the same restriction sites. Dendra2 was subsequently ligated into the pcDNA 3 vector. An analogous procedure was followed for pcDNA3.1 vector encoding for HRas-YFP. The integrity of the resulting reading frames was controlled by sequence analysis.

2.2.2 Cell culture and transfection

Mouse 3T3 fibroblasts were cultured in DMEM medium supplemented with 10% new born serum (NBS), streptomycin (200 μg/ml) and penicillin (200 U/ml) in a 7% CO_2 humidified atmosphere at 37 °C (95% humidity). Cells were transferred every 4 days. For microscopy, cells were cultured on 25 mm $\oslash$ glass slides, pretreated with hydrogen fluoride. Adherent cells were transfected with 1 μg DNA and 6 μl FuGENE 6HD (Roche

Diagnostic GmbH, Mannheim, Germany) per glass slide. The transfection efficiency, as determined by fluorescence microscopy, was about 20%. 1-3 days after transfection cells were fixed with 4% paraformaldehyde in phosphate buffer (PBS) (GIBCO, Invitrogen) at 37 °C for 15 minutes. For cholera toxin B (CTB) measurements cells were incubated with 5μg/ml Alexa647- cholera toxin B (Invitrogen) for 10 minutes prior to fixation.

2.2.3 Single-molecule fluorescence microscopy

PALM imaging was performed on a wide-field single-molecule imaging setup that has been described previously (16). In brief, 3T3 cells adherent to glass slide were mounted onto an inverted microscope (Axiovert100, Zeiss), equipped with a 100× oil immersion objective (NA 1.4, Zeiss), and kept in PBS at room temperature. The apical membrane of the cells was observed. For imaging the 514 nm line from an Ar/Kr laser (Spectra Physics) was coupled via an optical fiber into the excitation path of the inverted microscope. Light from a 405 nm diode laser (Crystal Laser, Reno, NV) was used to photoconvert Dendra2. Images were taken consecutively for up to at least 10^4 images per experiment. The time lag between images was set to 120 ms. Precise timing and intensity setting for the excitation light was achieved by an acousto-optic tunable filter (AA Electrooptique). The illumination intensity at 514 nm was set to 4 kW/cm^2 and the illumination time per frame to 5 ms. Both settings assured that most of the photoconverted Dendra2 molecules photobleached after one frame. The intensity of the 405 nm activation laser for photoconversion was increased from 0.2 μW/cm^2 to 20 μW/cm^{2}during acquisition, to ensure sufficient activation of fluorophores per frame. The density of photoconverted molecules was less than 0.1 molecule/μm^{-2}. The fluorescence was detected on a slow-scan back-illuminated CCD camera with pixel size of 20 μm which translates into a pixel size of 200 nm in the object plane. To correct for the drift of the setup, an immobilized fluorescent bead (Crimson Red FluoSpheres, 200 nm, Molecular Probes, Eugene, OR) was imaged simultaneously with the cells.

2.2.4 Image analysis

The signals of individual molecules (figure 2.1a) on the CCD were fitted to two-dimensional Gaussian profiles of mean full-width-at-half-maximum of 370±40 nm. The mean signal detected form an individual molecule

was 416±60 counts (figure 2.1b). The accuracy for single-molecule localization was found to be 35 nm (figure 2.1c). Subsequently all positions were corrected for experimental drift, determined to an accuracy of 5 nm by the fiducial bead positions analyzed separately. Dendra2 signals that lasted for longer than one frame or (re-)appeared within 500 frames, i.e. reappeared within 6 s, and were found within the positional accuracy were assumed to arise from the same molecule and discarded. The drift-corrected single-molecule positions were subsequently used to reconstruct a two-dimensional image of the cell membrane, as in figure 2.1d. Each position was thereby represented by a two-dimensional normal Gaussian of width given by the mean positional accuracy $\sqrt{\sigma_x^2 + \sigma_y^2}$ (see figure 2.2d). For each image $> 10^4$ positions were used.

2.2.5 Statistical analysis

For statistical analysis of potential non-random distributions of proteins on the plasma membrane we used Ripley's $L(r) - r$ function (19, 20):

$$L(r) - r = \sqrt{K(r)/\pi} - r \tag{2.1}$$

with Ripley's K-function K(r) that counts the mean number of neighbors in a distance of radius r from N points in an area A:

$$K(r) = \frac{A}{N^2} \sum_{i \neq j}^{N} w_{ij}^{-1} I_{\mathrm{r}}(d_{ij}) \tag{2.2}$$

d_{ij} is the Euclidean distance between two points and the counting measure $I_{\mathrm{r}}(d_{ij}) = 1$ if the distance $d_{ij} \leq r$, and $I_{\mathrm{r}}(d_{ij}) = 0$ otherwise. w_{ij} is a weighting factor that corrects for edge effects (19, 20). It corresponds to the proportion of the circumference of a circle with center in i and passing through j which lies within the area A.

For a spatially randomly arranged point-pattern $K(r) = \pi r^2$, and thus $L(r) - r$ approaches 0. For a non-random pattern with well-separated clusters of typical size R, $L(r) - r$ displays a characteristic maximum at R and decays to zero for large radii (21).

For analysis of the superresolution-images the cell's area, typically 7×7 μm^2, was split into square tiles of 1×1 μm^2. Each of the tiles contained at least 70 positions. $L(r) - r$ was analyzed for each tile separately. From those a mean $L(r) - r$ was calculated as well as a confidence interval

as defined by the $1 \cdot STD/\sqrt{realizations}$, where STD is the standard deviation of the different $L(r) - r$ realizations in each point of r.

2.2.6 Simulations

Point patterns were simulated using Matlab. As parameters we used values we found in our experiments and those reported in literature. The parameters were: concentration c ($5000 < c < 25000$ positions per $11 \times 11 \mu m^2$), fraction of randomly distributed molecules α ($0.4 < \alpha < 0.6$), number of clusters N_c ($10 < N_c < 200$), number of molecules per cluster, $p_c = c(1 - \alpha)/N_c$, (i.e. $7 < p_c < 30$), and cluster radius R (50 nm $< R <$ 500 nm). On top of randomly distributed position over the entire simulation area, N_c clusters were randomly distributed over the area, each containing p_c positions that were randomly distributed in a circular area of radius R surrounding these centers. $L(r) - r$ was calculated as in equation 2.1 for each realization, and the results were compared to the experimental ones. For a purely random distribution of positions ($\alpha = 0$) $L(r) - r$ fluctuates around zero. Further we found that for the case of clustering the position of the maximum of $L(r) - r$ is located close to the clustering radius R as was reported in (21), and the maximal value of $L(r) - r$ increases with the number of positions within a cluster p_c (for a summary of those simulations see appendix 4.A).

Two models were used in the simulation, a classical raft model and an alternative clustering model. For both models the study area was set to 11×11 μm, as in the experiments. The first model assumes a fix number of clusters N_c present in the membrane. As the total concentration of proteins is increased, a variable amount of molecules p_c is accommodate into the pre-existing clusters. The second model, instead, assumes a variable number of clusters, each containing the same amount of proteins p_c. As the total concentration is increased, new clusters are formed accordingly yielding: $N_c = C(1 - \alpha)/p_c$.

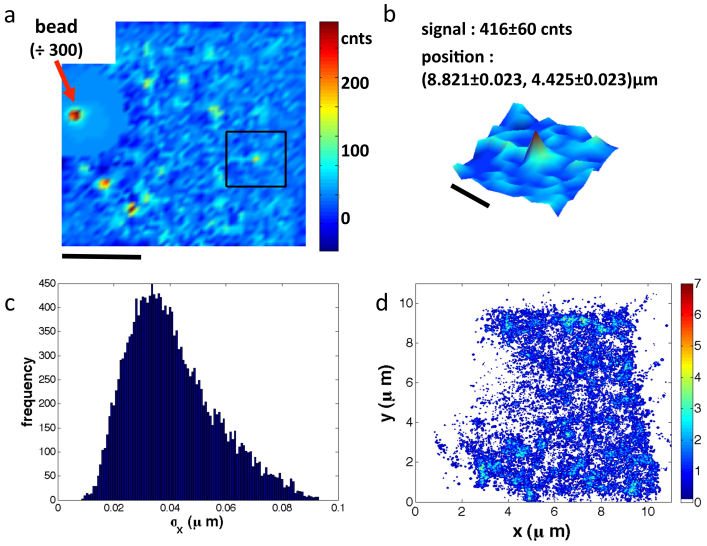

Figure 2.1: a) Single CAAX-Dendra2 signals. The signal of the bead used for drift correction is visible in the upper left corner. **b)** Gaussian fit of a single molecule signal. Average signal 461±60 counts per molecule. **c)** Positional accuracy along the x-direction. Mean $\sigma_x = 35$ nm. Analogous results was obtained in the y-direction, leading to a mean positional accuracy ~ 40 nm. **d)** Each position is represented as a 2-dimensional Gaussian and used to reconstruct CAAX distribution in the membrane.

2.3 Results

2.3.1 YFP-Acrylamide gel

The spatial distribution of randomly spaced molecules that was produced by immobilization of eYFP in a 15 % acrylamide gel was studied to validate our experimental strategy using Ripley's analysis. As shown by Biteen at al.(22), eYFP is reactivatable multiple times from the dark state, and thus it is a suitable fluorophore for superresolution imaging by PALM. 200 μl of 20 nM buffered solution of eYFP was diluted into 2 ml of polyacrylamide prior to polymerization. At this low final concentration of 2 nM the eYFP molecules were assumed to be randomly distributed. The sample was photobleached prior to measurement with continuos 514 nm illumination for 30 s at an intensity of 4 kW/cm^2. This photobleaching step assured that on average only one molecule per frame

was visible. Subsequently 1000 consecutive frames, 10×10 μm in size, were acquired in which we observed the stochastic recovery (22) and photobleaching of eYFP. In turn, the positions of the molecules in each frame were determined by fitting the intensity distribution from individual eYFP to a two-dimensional Gaussian (see section 2.2). Eight separate areas of the gel where imaged, with an average of 13 eYFP molecules/μm^2. To reconstruct a high resolution image each molecule was plotted as a two-dimensional Gaussian with standard deviation that equals the positional accuracy, $\langle \sigma_{1D} \rangle = 35$ nm (see figure 2.2 a). The resulting image shows a random distribution of molecules throughout the region of interest (figure 2.2b). An analysis based on Ripley's $L(r) - r$ function was performed to confirm the latter visual inspection. The observed area was divided into non-overlapping tiles of 1×1 μm^2 in size, and $L(r) - r$ was evaluated in each box up to a radius $r = 0.5$ μm. The mean of all 8 independent measurements together with their confidence interval (see section 2.2) is shown in figure 2.2c. The data fall into the range of a randomly distributed sample that has been predicted from our simulations using the same number of data points (figure 2.2c, light gray area). Hence, these control experiments validate the chosen approach to detect a random distribution by means of super-resolution microscopy in conjunction with Ripley's analysis.

2.3.2 CAAX

Initially we studied the membrane distribution of the minimal anchoring motif of HRas, CAAX, in the inner leaflet of the plasma membrane. The CAAX sequence consists of 10 amino acids, three of which are cysteines, to which one S-prenyl and two S-acyl groups are posttranslationally attached (11, 13). Association of CAAX to membrane domains that have a size between 20 and 200 nm has been suggested earlier using various indirect methods (17). Here we performed super-resolution experiments to directly visualize those potential domains on cells that where fixed prior to imaging. Mouse 3T3 fibroblasts were transfected with a construct that codes for the CAAX-sequence fused to the photoconvertible dye Dendra2. In these, and all the subsequent experiments, we chose to use the photoconvertible label Dendra2 as compared to eYFP used in the control experiments in gel. Dendra2 offers an active regulation of the photoconversion and does not require the high fluence photobleaching step that might cause damage to the cell sample. Wide-field and confocal images showed that the construct was faithfully located at the membrane (not shown), as

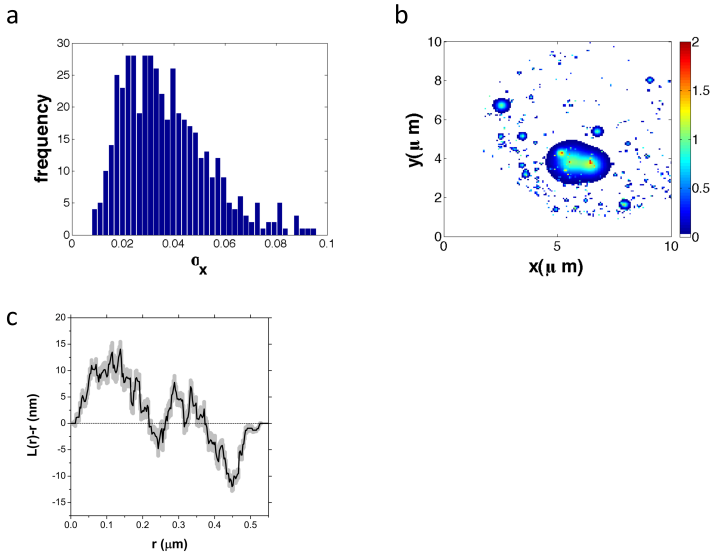

Figure 2.2: **a)** One dimensional positional accuracy along the x-axis for single YPF molecules. Mean σ_x=30 nm. **b)** Each position is represented as a 2-dimensional Gaussian and used to reconstruct YFP distribution in the gel. **c)** $L(r) - r$ calculated for the YFP gel. The function fluctuates around zero, as expected for a random distributed sample. Grey area: confidence interval.

reported earlier for the CAAX-eYFP construct (17). The localization of CAAX was studied in 10 cells. Prior to super-resolution imaging a bright-field image was taken to select a cell and define a region of interest on it's apical membrane. High resolution fluorescence images were taken for up to 25000 frames per sequence. The activation laser intensity was varied between 0.2 and 20 μW/cm^2 during acquisition to ensure that, on average, 2 to 10 molecules were activated per frame. For the analysis single fluorophore positions were localized and selected as described in section 2.2. All the molecules' positions were subsequently used to create super-resolution images of CAAX-distributions on the plasma membrane (figure 2.3a). From such images it appeared obvious that CAAX was not homogeneously distributed on the apical plasma membrane. Irregular patches containing high density of molecules (bright red areas in figure 2.3a) of size in the range $50 - 200$ nm were visible alternated with regions of sparsely distributed molecules (blue areas).

To analyze more rigorously the CAAX's distribution, we performed

statistical analysis based on Ripey's K-function. Analysis was implemented iteratively on 1×1 μm^2 tiles, covering the entire cell. Tiles that contained more than 70 molecules (ranging from 78 to 711 molecules/μm^2) were subsequently used for Ripley's analysis. $L(r) - r$ was calculated for each tile. The resulting curves per tile were averaged to obtain a single $< L(r) - r >$ curve representative for the distribution in a single cell (figure 2.3 b).The tiling further allowed us to obtain an experimental estimate of the confidence-interval for the averaged Ripley's $< L(r) - r >$ function for each measurement. Finally the average and confidence interval for all 10 cells were calculated to also include potential biological variability of the data set. The cells-averaged curve was taken as representative of CAAX distribution on the plasma membrane in 3T3 fibroblast cells (figure 2.3c). This statistical analysis corroborates the visual imaging results and shows a strongly clustered partitioning of CAAX on the membrane. $L(r) - r$ is larger than zero on the full interval the analysis has be performed on and is larger than the confidence interval of a random sample between 80 and 450 nm. It displays a maximum of $L_{\max}^{\mathrm{CAAX}}$=28$\pm$3 nm, that is located at $r_{\max}^{\mathrm{CAAX}}$=218$\pm$23 nm. The errors in $L_{\max}^{\mathrm{CAAX}}$ and $r_{\max}^{\mathrm{CAAX}}$ were calculated as standard-error of the mean from the different single-cells measurement, respectively. The value of $r_{\max}^{\mathrm{CAAX}}$ represents the length-scale at which clustering occurs. The fairly wide range at which $L(r) - r$ peaks is indicative of the presence of a wide distribution of cluster size between $100 - 300$ nm (figure 2.3c, see also appendix 4.A).

These results support the hypothesis that the membrane anchor of HRas is responsible for partitioning of HRas into domains along the plasma membrane. To further study the nature of these domains, we analyzed the variation of the maximum of $L(r) - r$ at increasing protein concentration. For this analysis we utilized the fact that CAAX expression was variable in the cell pool analyzed between 78 and 711 molecules/μm^2. As shown in figure 2.3d, $L_{\max}^{\mathrm{CAAX}}$ remains constant over a broad range of concentrations indicating that the number of molecules per cluster stays constant.

In summary, our data suggest that the membrane anchor CAAX dynamically partitions into membrane domains, forming clusters of proteins of a few hundreds of nanometer in radius.

2.3.3 HRas

Subsequently we studied the full protein HRas. HRas was fused to the photoconvertible fluorescent protein Dendra2 and expressed in 3T3 fibrob-

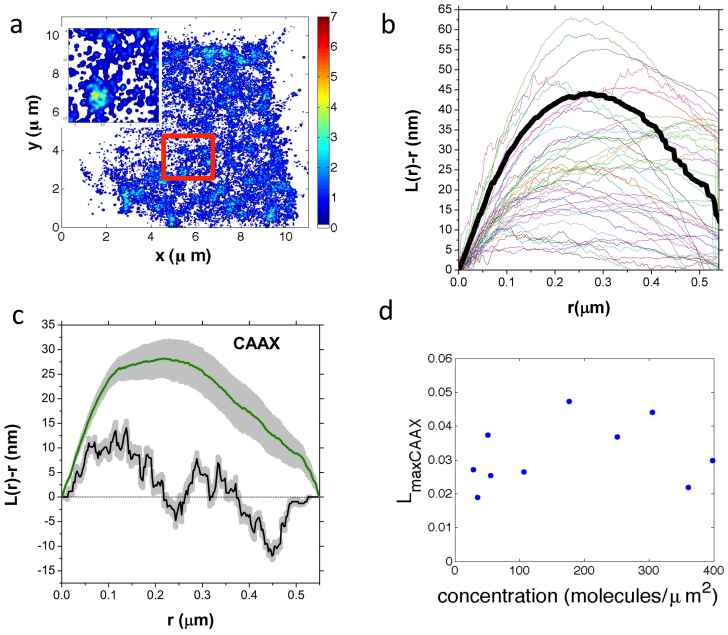

Figure 2.3: a) Each position is represented as a 2-dimensional Gaussian and used to reconstruct CAAX distribution in the membrane. Insert show a zoom in the image (red square) where clusters are visible. **b)** $L(r)-r$ calculated for a single cell. The image is divided into tiles and $L(r) - r$ is calculated for each. The resulting average curve (thick black line) is taken as represantative of CAAX distribution within the cell. **c)** The final curves obtained from 10 cells were averaged (solid blue line) and further analyzed. Positive deviation from zero (dotted line) is observed starting from r=80 nm and reaching a maximum at $r_{\max}^{\mathrm{CAAX}} = 218$ nm. The gray area is the confidence interval, corresponding to one standard deviation from the average of the 10 curves. Black thin line: results from YFP-gel. **d)** Maximum of $L(r) - r$ as a function of protein concentration. There is weak dependence of the maximum on concentration, indicating a dynamic clustering of CAAX into domains.

lasts. The fusion protein was faithfully targeted to the plasma membrane as analyzed by confocal imaging (data not shown). The expression level of HRas-Dendra2 ranged from 50 to 1100 molecules/μm^2, comparable to that we found for CAAX-Dendra2. This allows a direct comparison of the resulting curves. The reconstructed high-resolution images of HRas exhibit large aggregates, connoting a non-random distribution of HRas on the plasma membrane (figure 2.4a). Statistical analysis by Ripley's $L(r) - R$ function highlights the high similarity between the HRas distri-

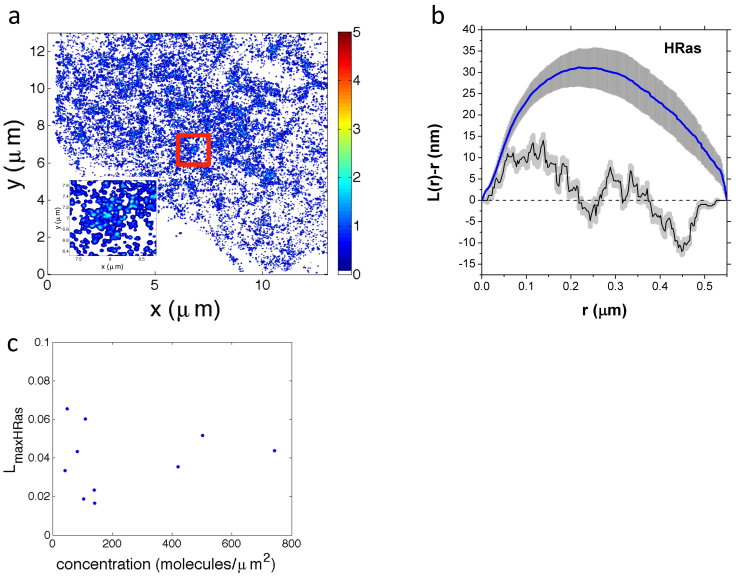

Figure 2.4: **a)** Each position is represented as a 2-dimensional Gaussian and used to reconstruct HRas distribution in the membrane. Insert show a zoom in the image (red square) where clusters are visible. **b)** The final curves obtained from 10 cells were averaged (solid blue line) and further analyzed. Positive deviation from zero (dotted line) is observed starting from r=80 nm and reaching a maximum at $r_{\max}^{\mathrm{HRas}} = 220$ nm. The gray area is the confidence interval, corresponding to one standard deviation from the average of the 10 curves. Black thin line: results from YFP-gel. **C)** Maximum of $L(r) - r$ as a function of protein concentration. There is weak dependence of the maximum on concentration, indicating a dynamic clustering

bution with that of it's membrane anchor CAAX (figure2.4b). The maximum of $L(r) - r$ for HRas, $L_{\max}^{\mathrm{HRas}}$=31±4 nm is located at $r_{\max}^{\mathrm{HRas}}$=220±10 nm as shown in figure 2.4b. The analysis of clustering the maximum $L_{\max}^{\mathrm{HRas}}$ of HRas as a function of protein expression does not depend on protein concentration, equivalent to our finding on the protein's membrane anchor CAAX (see figure 2.4c).

These findings suggest a major role for the anchoring motif of HRas on its targeting and organization into membrane domains on the cytosolic side of the plasma membrane.

2.3.4 Cholera toxin B treatment

In a last set of experiments we were to investigate whether the membrane domains on the cytosolic leaflet of the plasma membrane could be induced or manipulated by the organization of lipids in the outer leaflet of the plasma membrane. Therefore cells were treated with cholera toxin subunit B (CTB). CTB binds up to five ganglioside GM1 molecules in the outer leaflet of the plasma membrane. It has been shown by Lingwood (24) that CTB induces a cholesterol-dependent coalescence of GM1-containing domains in plasma membrane blebs at physiological temperature. Our hypothesis was that if HRas and it's membrane anchor were coupled to cholesterol enriched domains in the outer leaflet, the incubation of cells with CTB would induce a variation in their spatial distribution. Thus, a change in $L(r) - r$ upon CTB-treatment would be an evidence of coupling between inner and outer leaflet of the plasma membrane.

Cells were incubated with Alexa-647 conjugated to CTB for 10 minutes at 37° C prior to fixation. The short incubation time was necessary to prevent endocytosis and internalization of the toxin. Cells were imaged with a 639 diode-laser to visually control toxin binding and ensure that CTB was not internalized. Cells were imaged and analyzed as described above. $L(r)-r$ of both CAAX and HRas before and after the treatment were compared. Upon CTB incubation CAAX-Dendra2 transfected cells exhibit a significant change in $L(r) - r$ as shown in figure 2.5a. The maximum value of $L(r) - r$ increases from $L_{\max}^{\mathrm{CAAX}}$=28±3 nm to 36±2 nm after CTB treatment (see figure 2.5c). The position of the maximum, $r_{\max}^{\mathrm{CAAX}}$=220±25 nm appeared to be smaller after treatment, $r_{\max}^{\mathrm{CAAX}}$=198±10 nm (see figure 2.5d). A different effect was observed for HRas-Dendra2 as shown in figure 2.5b. The maximum value of $L(r) - r$ increases to $L_{\max}^{\mathrm{HRas}}$=33 ±5 nm. This change however falls into the confidence interval of the measurements prior to CTB treatment (see figure 2.5c). Surprisingly the position of the maximum changed from $r_{\max}^{\mathrm{HRas}}$=220±10 nm before to $r_{\max}^{\mathrm{HRas}}$=238 ±11 nm upon toxin application (see figure 2.5d). This latter finding suggests that cluster size increases significantly for the full protein but not for it's membrane anchor. The increase in maximum value of $L(r) - r$ for both the membrane anchor as well as for the full HRas protein suggests an accumulation of proteins per cluster upon CTB treatment.

These results provide further evidence of the existence of a coupling between domains in the cytosolic side of the membrane and the lipids organization on the outer leaflet of the plasma membrane.

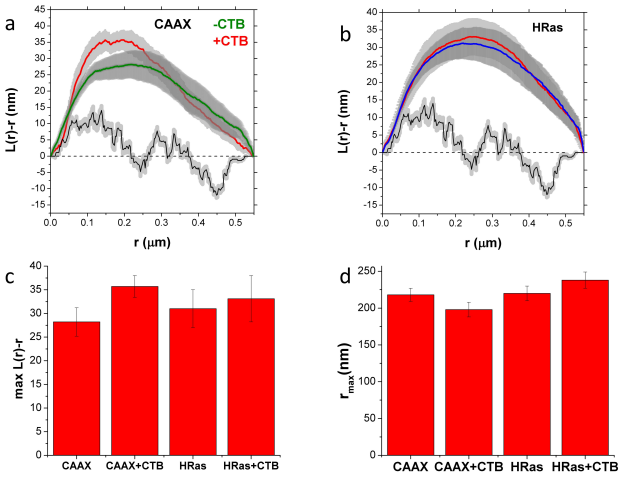

Figure 2.5: a) CAAX distribution before (blue line) and after (red line) treatment with CTB. An increase in the maximum value of $L(r) - r$ is observed upon toxin treatment.**b)** HRas distribution before (green line) and after CTB treatment (red line). A steep increase in the maximum value of $L(r) - r$ is observed. Both CAAX and HRas show maximum clustering at approximately $r_{\max} \sim 230$ nm. Treatment with CTB induces a reorganization of the protein in the plasma membrane, causing an increase in clustering for both CAAX and HRas. The radius of maximal clustering remains unchanged. **c)** Maximum value of $L(r) - r$ for CAAX and HRas before and after CTB treatment. **d)** Radius of maximum clustering for CAAX and HRas before and after CTB treatment.

2.3.5 Simulations results

The data presented above demonstrate that HRas and its membrane anchor CAAX is not homogeneously distributed in the plasma membrane. To quantitatively interpret our findings we performed a set if simulations to narrow down the parameter values of clustering models that were able to reproduce the experimental pattern reported in figures 2.3 and 2.4.

First, we test whether the position of the maximum is representative of the real cluster size. The cluster radius was varied between 11 and 300 nm, and for each radius 20 simulations were performed. The position of the maximum slightly overestimates the real cluster size. For details see appendix 4.A.

Subsequently, we simulated patterns in the range 20-250 molecule/μm^2 to find the set of parameters which could best reproduce the data. In

these simulations the total number of molecules expressed was varied in the range found in the experimental data, c=5000-25000. A fraction α of molecules were distributed in a pool of randomly distributed molecules, $N_{\mathrm{r}} = \alpha c$, and a pool of size $N_{\mathrm{d}} = (1-\alpha)c$ molecules that resides in domains. The radius of the simulated circular domains was set to match the position of the maximum of the experimental $L(r) - r$ ($r_{\max} = 218$ nm) corrected for the overestimate introduced by the analysis. The simulations reproduced the experimental radius of maximum clustering , however the distribution was narrower as compared to CAAX and HRas (see figure 2.6a). When additionally allowed for an eccentricity $\epsilon = 0.6$ and a distribution of radii of 70-300 nm the data were closely reproduced (figure 2.6a). For each concentration a set of 20 simulations were run, and $L(r) - r$ was evaluated. The model assumed that the number of molecules per cluster, p_{c} was constant. Hence, the number of clusters varied as $N_{\mathrm{c}} = N_{\mathrm{d}}/p_{\mathrm{c}}$. With this approach the parameters which best describe the data are given by: α=0.6 (40% of the molecules are confined in clusters), and p_{c}=15 molecules/cluster. This set reproduces correctly both the experimental position of $L(r) - r_{\max}$ and the value of $L(r) - r$. The same model was used to model the effect of CTB on the membrane anchor distribution (figure 2.6b). We found that CTB induce an increase of molecules/cluster, p_{c}=25, however the total fraction α of clustered molecules remains unchanged.

2.4 Discussion

The differential activity of the various isoforms of Ras proteins has been suggested to result from protein localization in separate membrane compartments. This partitioning is supposed to be mediated by the different C-terminal membrane anchoring sequences. Interestingly it has been found that partitioning is connected to the activation state of Ras proteins (18) thus hinting to a functional role of membrane partitioning in protein function. Here we studied the membrane distribution of HRas and its membrane anchoring motif CAAX in 3T3 fibroblats by direct super-resolution imaging. Our data show that both the minimal anchoring motif CAAX and the full protein HRas are not homogeneously distributed in the plasma membrane of 3T3 cells but rather are localized in part into domains. Our results hence further confirm the presence of membrane domains in the inner leaflet of the membrane. The spatial distributions

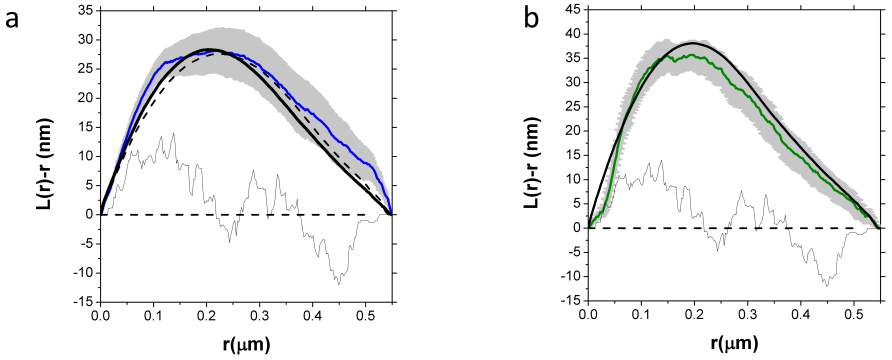

Figure 2.6: a) Experimental $L(r)-r$ (blue line) compared to the best fitting simulations. Dashed black line: simulation of circular domains with radius r=218 nm. The curve reproduces the position and value of the maximum of the experimental data, but fails at shorter value of r. Solid black line: $L(r) - r$ calculated from simulated point pattern with elliptical domain, varying in radius between 70 and 200 nm. **b)** Experimental $L(r) - r$ for CAAX transfected cells treated with CT. Black line: simulation reproducing the experimental results. As for non-treated cells the data are best fitted using elliptical clusters and a distribution of domains radii. p_c is ~ 2 times higher than for CAAX.

between HRas and that of it's membrane targeting sequence CAAX we found to be highly similar. This finding further support the notion that localization of the Ras proteins in the plasma membrane is largely controlled by their membrane anchor.

In previous single-molecule tracking experiments it has been found that a fraction of $\sim 40\%$ of both HRas and it's membrane anchor CAAX exhibited a slowly diffusing fraction that was confined to domains of ~ 220 nm size (17). Likewise immuno electron-microscopy imaging of ripped membranes showed that 36% of HRas was localized inside of domains (23). Our results here quantitatively corroborate those findings. The spatial distributions obtained from our data were reproduced in simulations in which a ratio of domain-bound to randomly positioned molecules of 2/3 was assumed. This similarity in fraction size suggests that we can identify the fast diffusing fraction that was found in single-molecule tracking experiments with the randomly distributed proteins in the super-resolution images, and that the slow, confined diffusing fraction is identical to the domain-localized fraction.

The wide distributions we found for the spatial correlation is an indi-

cation for a wide distribution of domain sizes that span from 80-250 nm as estimated from our simulations. The upper limit of the domain-size distribution thereby is in agreement with the domain sizes that had been inferred from single-molecule tracking experiments of ∼220 nm (17). The direct imaging by super-resolution microscopy combined with spatial distribution analysis allowed us, however, to unravel the more complex partitioning behavior, where bigger domains coexist with smaller domains, potentially in a dynamic equilibrium. It probably is impossible to unravel such data using the earlier approaches by single-molecule tracking due to the spatial averaging required in the latter experiments. The lower bound of 80 nm reported is in agreement with the domain size as obtained by immuno electron microscopy when taking into account our limited positional accuracy of $\sigma = 35$ nm. The positional accuracy will increase any real domain size, r_{real} by $\sqrt{2}\sigma$ leading to a real domain dimension, as inferred from the lower bound of 80 nm, of 30 nm. This finding is within a factor of two equal to the value reported in EM of ∼12 nm (10, 23).

By studying the maximum value of the spatial distributions, $L_{\max}$, at increasing expression level we were able to discriminate between two potential clustering models. Both HRas and the membrane anchor CAAX likely partition into dynamically forming domains that have a rather constant protein density. The model of preexisting, long lasting domains into which an increasing amount of molecules partition is not able to explain our experimental findings, and can hence be rejected. It is interesting to note that this model applies to both the anchor and the full HRas protein, supporting further the view that the anchoring motif is responsible not only for membrane targeting, but as well is a signal for the selective recruitment of the protein to membrane domains.

Prior studies have suggested that HRas is localized in cholesterol-enriched raft domains. Our data here in part corroborate this association. It is well established that the ganglioside GM1 resides in cholesterol-rich domains in the plasma membrane. The incubation of cells with cholera-toxin B that crosslink GM1 on the extracellular leaflet is supposed to coalesce and increase raft-domains that can be up to micrometer in size for membrane blebs detached from the cell body (24). Our results show that CTB treatment induces an enrichment of proteins concentration into domains as observed by the increase of $L_{\max}$ in figure 2.5. However, we also found that the total fraction of molecules that partitioned into the domains, and the size of the domains remained unchanged. The formation of

nanoclusters in the inner leaflet, however, cannot be explained completely by cholesterol-enriched domains, since size and amount of clusters remains unchanged upon CTB treatment. This conclusion is supported by previous extraction experiments, which did not effect the stability of membrane domains (17). An attractive option is to identify the actin cytoskeleton as a player in domain formation, which could also explain the distribution of cluster sizes observed. These results reflect on one side the role played by cholesterol in membrane-anchored proteins organization and distribution, and on the other had they prove the existence of an interaction between the inner and outer leaflet organization.

In conclusion, we suggest a model for inner membrane partitioning in dynamic domains, varying in size from a few tens to hundreds of nanometer in diameter. HRas partition dynamically in and out of those domains, and its localization is determined primarily by the anchoring motif CAAX. This differential localization is mediated by the lipid composition and organizations both in the inner and outer leaflet. A coupling between the leaflets has also been shown, as reorganization at the extracellular side led to protein enrichment of microdomains in the inside.

2.A Appendix

2.A.1 Estimation of radius of maximum clustering

As reported by Kenworthy et al. (21), the position of the maximum of $L(r) - r$ is a good estimate for the radius of maximum clustering. To validate this assumption, we performed a series of simulation varying the clustering radius. Fixed parameters in the simulations were: randomly distributed molecules Nr=5000 molecules/cluster, number of clusters Nc=600, and the number of protein per cluster Np=15 molecules/cluster. The radius of maximum clustering was varied between 22 and 200 nm. As shown in figure2.7b-c, the position of the maximum of $L(r) - r$ tends to slightly overestimate the real cluster size, in agreement with (21).

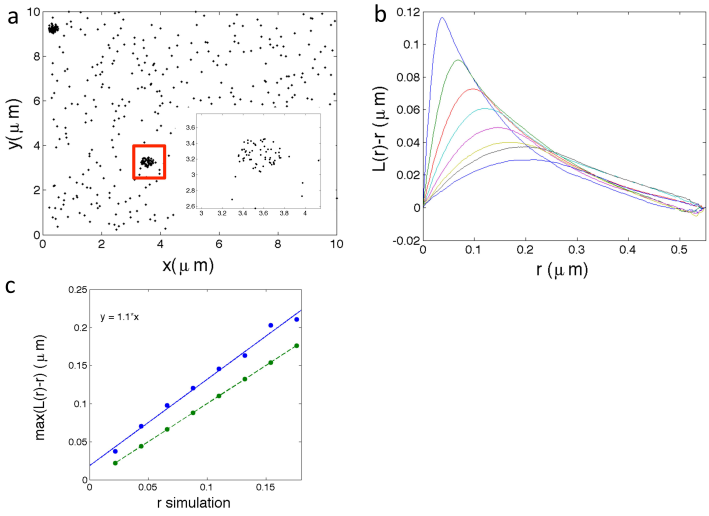

Figure 2.7: a) Example of a simulated point pattern. Two clusters with ~ 60 molecules are visible. Clustering radius $r = 200$ nm. From graphical inspection we confirm that the chosen radius corresponds to outcome of the simulation.**b)** $L(r) - r$ was evaluated for each simulation. As the radius increases the maximum of the curves shift toward higher radii and lower value of $L_{\max}$.**c)** Blue solid line: position of the maximum of $L(r) - r$ as a function of the clustering radius. Green dotted line: actual domains radius, as set in the simulations.

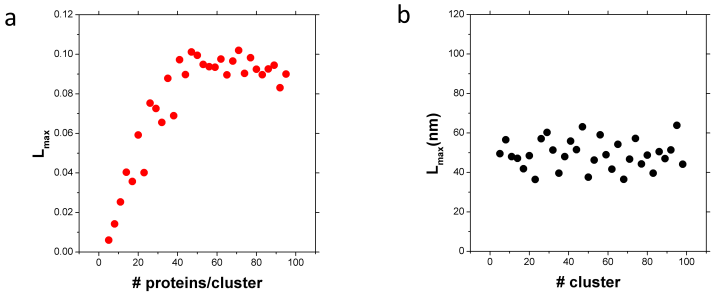

Figure 2.8: **a)** Maximum of L(r)-r as a function of the number of protein/cluster.**b)** Maximum of L(r)-r as a function of the number clusters.

2.A.2 Clustering models

Two different clustering models were tested. The first, a classical clustering model, assumes a constant number of clusters at different concentrations of molecules. Increasing the concentration results in an enrichment of the amount of molecules per cluster. Constant parameters in the simulations were: number of random positions, $Nr = 600$, number of clusters, $N_c = 20$, clustering radius, $r = 50$ nm, and image size, 20×20 μm. Variable parameter was the number of protein per cluster, that varied in range $n_p = 5 - 100$ protein/cluster. $L(r) - r$ was calculated for each condition and its maximum value was retrieved. As depicted in figure 2.8a the maximum of $L(r) - r$ increases protein concentration.

The second model assumes a constant number of proteins per clusters. As concentration increases, new clusters are formed. Constant parameters in the simulations were: number of random positions, $Nr = 600$, number of proteins per cluster, $N_p = 20$, clustering radius, $r = 50$ nm, and image size, 20×20 μm. Variable parameter was the number clusters, that varied in range $n_p = 5 - 100$ clusters. $L(r) - r$ was calculated for each condition and its maximum value was retrieved. According to this model, the maximum value of $L(r) - r$ does not vary as a function of the concentration, as shown in figure 2.8b.

Bibliography

[1] Lommerse, Spaink, H.P., Schmidt, T. (2004), In vivo plasma membrane organization: results of biophysical approaches. *BBA* **1664**,119-131.

[2] Prior, I. A., Harding, A., Yan, J., Sluimer, J., Parton, R. G. and Hancock, J. F. (2001). GTP-dependent segregation of H-ras from lipid rafts is required for biological activity. *Nat. Cell. Biol.* **3**, 368-375.

[3] Yechiel, E., Edidin, M. (1987) Micrometer-scale domains in fibroblast plasma membranes.*J.Cell.Biol.***105**,755-760.

[4] Kenworthy, A.K., Edidin, M. (1999) Imaging fluorescence resonance energy transfer as probe of membrane organization and molecular associations of GPI-anchored proteins. *Methods Mol. Biol.* **116**, 37-49.

[5] Korlach, J., Schwille, P., Webb, W., and Feigenson, G. (1999) Characterization of lipid bilayer phases by confocal microscopy and fluorescence correlation spectroscopy.*Proc.Natl.Acad.Sci.USA*, **96**, 8461-8466.

[6] Chiantia, S., Ries, J., Schwille, P. (2009) Fluorescence correlation spectroscopy in membrane structure elucidation. *BBA* **1788**, 225-233.

[7] Eggeling, C., Ringemann, C., Medda, R., Schwarzmann, G., Sandhoff, K., Polyakova, S., Belov, V.N., Hein, B., von Middendorff, C., Schonle, A., Hell, S.W. (2009) Direct observation of the nanoscale dynamics of membrane lipids in a living cell. *Nature* **457**, 1159-1162.

[8] Pralle, A., Keller, P., Florin, E.L., Simons, K., Hï¿½rber, J.K. (2000) Sphingolipid-cholesterol rafts diffuse as small entities in the plasma membrane of mammalian cells. *J.Cell.Biol.* **148**, 997-1008.

[9] Murase, K., Fujiwara, T., Umemura, Y., Suzuki, K., Iino, R., Yamashita, H., Saito, M., Murakoshi, H., Ritchie, K., Kusumi, A. (2004) Ultrafine membrane compartments for molecular diffusion as revealed by single molecule techniques. *Biophys.J.* **86**, 4075-4093.

[10] Prior, I. A., Muncke, C., Parton, R. G. and Hancock, J. F. (2003). Direct visualization of Ras proteins in spatially distinct cell surface microdomains. *J.CellBiol.* **160** 165-170.

[11] Hancock, J. F., Paterson, H. and Marshall, C. J. (1990). A polybasic domain or palmitoylation is required in addition to the CAAX motif to localize p21Ras to the plasma membrane. *Cell*, **63**, 133-139.

[12] Hancock, J. F., Cadwallader, K., Paterson, H. and Marshall, C. J. (1991). A CAAX or a CAAL motif and a second signal are sufficient for plasma membrane targeting of ras proteins. *EMBO J.*, **10**, 4033-4039.

[13] Apolloni, A., Prior, I. A., Lindsay, M., Parton, R. G. and Hancock, J. F. (2000). H-ras but not K-ras traffics to the plasma membrane through the exocytic pathway. *Mol. Cell. Biol.*, **20**, 2475-2487.

[14] Choy, E., Chiu, V. K., Silletti, J., Feoktistov, M., Morimoto, T., Michaelson, D., Ivanov, I. E. and Philips, M. R. (1999). Endomembrane trafficking of ras: the CAAX motif targets proteins to the ER and Golgi. *Cell*, **98**, 69-80.

[15] Alberts, B., Johnson, A., Lewis, J., Raff, M., Roberts, K., and Walter, P. (2007) Molecular biology of the cell. *Garland Science, New York.*

[16] Harms, G. S., Cognet, L., Lommerse, P. H., Blab, G. A., Schmidt, T. (2001). Autofluorescent proteins in single-molecule research: Applications to live cell imaging microscopy. *Proc. Nat. Acad. Sci.* **80**, 2396 - 2408.

[17] Lommerse, P. H. M., Blab, G. A., Cognet, L., Harms, G. H., Snaar-Jagalska, B. E., Spaink, H.P., Schmidt, T. (2004) Single-Molecule Imaging of the H-Ras Membrane Anchor Reveals Domains in the Cytoplasmic Leaflet of the Cell Membrane. *Biophys.J.* **86**, 609-616.

[18] Lommerse, P. H. M., Snaar-Jagalska, E. B., Spaink, H. P., and Schmidt, T. (2005) Single-Molecule Diffusion Measurements of H-Ras at the Plasma Membrane of Live Cells Reveal Microdomain Localization Upon Activation. *J. Cell Sci.*, **118**, 1799-1809.

[19] Ripley, B.D. (1977) Modeling Spatial Patterns *J.R.Stat.Soc.B* **39**, 172-192.

[20] Besag, J. E. (1977) *J.R.Stat.Soc.B* **39**, 193-195.

[21] Kiskowski, M. A., Hancock, J. F., Kenworthy, A. K. (2009) On the use of Ripley's K-function and its derivatives to analyze domain size. *Biophys.J.* **97**, 1095-1103.

[22] Biteen, J. S., Thompson, M. A., Tselentis, N. K., Bowman, G. R., Shapiro, L., Mowrner, W.E. (2008), Super-resolution imaging in live Caulobacter crescentus cells using photoswitchable EYFP. *Nat.Meth.* **5**, 947-949.

[23] Plowman, S. J., Muncke C., Parton, R. G., Hancock, J. F. (2005) H-ras, K-ras, and inner plasma membrane raft proteins operate in nanoclusters with differential dependence on the actin cytoskeleton. *Proc.Natl.Acad.Sci.USA* **102**, 15500-15505.

[24] Lingwood, D., Ries, J., Schwille, P., Simons, K. (2008) Plasma membranes are poised for activation of raft phase coalescence at physiological temperature. *Proc.Natl.Acad.Sci.USA* **105**, 10005-10010.

[25] Wolf, A. A., Jobling, M. G., Saslowsky, D. E., Kern, E., Drake, K. R., Kenworthy, A.K., Holmes, R.K., Lencer, W. I. (2008) Attenuated Endocytosis and Toxicity of a Mutant Cholera Toxin with Decreased Ability To Cluster Ganglioside GM1 Molecules *Infection and Immunology* **76**, 1476-1484.